DOI: 10.61782/fa.2023.0342

forum acusticum 2023

LOW FREQUENCY ABSORPTION BY 3D PRINTED MATERIALS HAVING HIGHLY TORTUOUS LABYRINTHINE SLITS IN IMPERMEABLE OR MICROPOROUS SKELETONS

Tomasz G. Zieliński[1*] **Kamil C. Opiela**[1] **Nicolas Dauchez**[2]
Thomas Boutin[2] **Marie-Annick Galland**[3] **Keith Attenborough**[4]

[1] Institute of Fundamental Technological Research, Polish Academy of Sciences, ul. Pawińskiego 5B, 02-106 Warsaw, Poland

[2] Université de Technologie de Compiègne, Alliance Sorbonne Université, Laboratoire Roberval, Centre de recherche Royallieu, CS 60319, 60203 Compiègne CEDEX, France

[3] Laboratoire de Mécanique des Fluides et d'Acoustique, Université de Lyon, École Centrale de Lyon, INSA Lyon, Université Claude Bernard Lyon I, CNRS, UMR 5509, 36 Avenue Guy de Collongue, F-69134, Ecully, France

[4] The Open University, School of Engineering and Innovation, Milton Keynes MK7 6AA, UK

ABSTRACT

The low frequency peaks in the absorption spectra of layers of conventional porous materials correspond to quarter wavelength resonances and the peak frequencies are determined essentially by layer thickness. If the layer cannot be made thicker, the frequency of the peak can be lowered by increasing the tortuosity of the material. Modern additive manufacturing technologies enable exploration of pore network designs that have high tortuosity. This paper reports analytical models for pore structures consisting of geometrically complex labyrinthine networks of narrow slits resembling Greek meander patterns. These networks offer extremely high tortuosity in a non-porous solid skeleton. However, additional enhancement of the low frequency performance results from exploiting the dual porosity pressure diffusion effect by making the skeleton microporous with a significantly lower permeability than the tortuous network of slits. Analytical predictions are in good agreement with measurements made on two samples with the same tortuous slit pattern, but one has an impermeable skeleton 3D printed from a photopolymer resin and the other has a microporous skeleton 3D printed from a gypsum powder.

Keywords: *sound absorption, high tortuosity, dual porosity, 3D printed materials.*

**Corresponding author*: *tzielins@ippt.pan.pl.*

1. INTRODUCTION

Traditional porous materials are only able to effectively absorb low-frequency sound when very thick layers are used. This is mainly because at lower frequencies the speed of sound in highly porous materials is only slightly slower than in the open air, while the first absorption peak is associated with the quarter wavelength resonance, i.e. when the layer thickness equals one quarter of the wavelength in the porous material. Therefore, for such porous layers of low or medium thickness, this absorption peak appears at high or medium frequency, where the wavelengths are shorter in general, and in the porous material much shorter than in the open air. The way to improve this is to somehow reduce the effective speed of sound in the material at lower frequencies. This can be achieved by in-

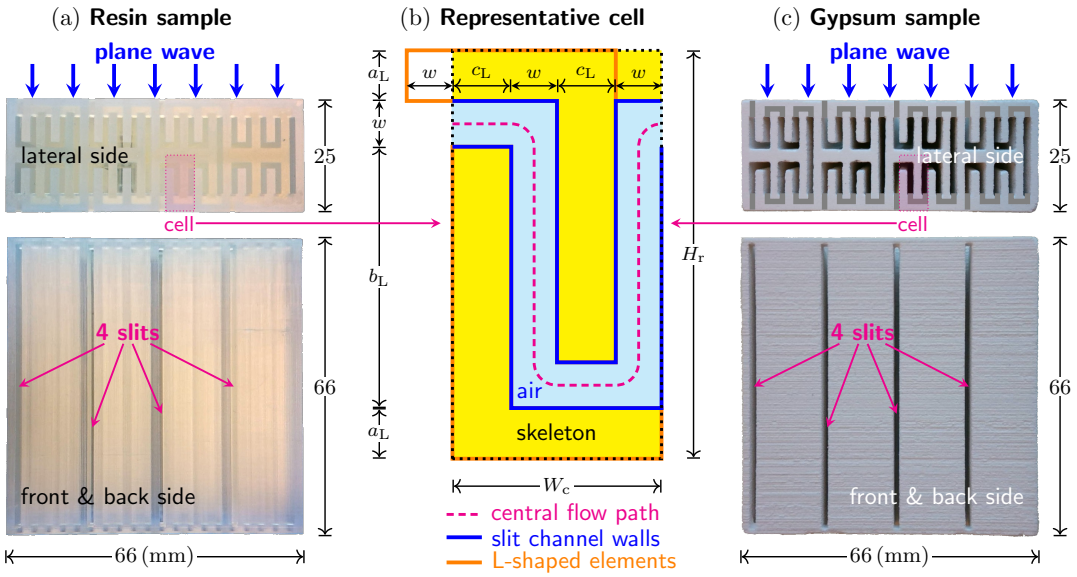

Figure 1. 3D printed samples of acoustic panels (views of their ensonified front or back side and open lateral side) with highly tortuous networks of slits with geometry specified by the same representative cell.

creasing the tortuosity of the porous material to lengthen the path of the associated viscous airflow in the material [1].

The tortuosity of conventional acoustic foams and fibrous materials is low (typically between 1 and 3) and only new designed materials can provide very high tortuosity values. Recently proposed solutions are structures with coiled-up cavities [2] and materials with labyrinthine perforations [3]. This work investigates acoustic panels with labyrinthine slits of essentially two-dimensional design. In the more efficient case, the skeleton of the panel is microporous, although the micropores are small enough to ensure a high permeability contrast with the main network of slits and thus its high tortuosity as viscous leakage through the micropores is not allowed. Moreover, an additional wave-attenuation mechanism of pressure diffusion is introduced in this way [4].

Analytical modelling of such dual-porosity materials with labyrinthine slits as well as their single-porosity version with an impermeable skeleton is discussed in detail and used to design sample panels. Two different additive manufacturing technologies are used to 3D print these samples. The sample of dual-porosity panel is 3D printed from gypsum powder providing a microporous skeleton, while the single-porosity sample has an impermeable skeleton made of resin but the same network of labyrinthine slits. The sound absorption measured for both samples is compared with each other and confronted with the predictions resulting from analytical modelling.

2. PANELS WITH LABYRINTHINE SLITS

2.1 3D printed samples

Figure 1 shows two $66\times66\times25$ mm samples of sound absorbing panels with highly tortuous labyrinthine slits and the geometry of a representative cell that allows to analyse such panels. The samples were 3D printed from two completely different materials, and consequently, in two essentially different additive manufacturing technologies [5], namely: (1) from a photopolymer resin – in Stereolithography (SLA), and (2) from a coarse gypsum powder – in Binder Jetting 3D Printing (BJP) using butyrolactam as binder. The resin sample (Figure 1a) is of very high quality in terms of mapping the designed geometry as well as surface smoothness, while the gypsum-based sample (Figure 1c) has rough surfaces and many albeit rather minor geometrical imperfections. It is known, however, that such imperfections, and especially surface roughness, should rather enhance the sound absorbing properties [6, 7]. More importantly, it was found that the skeleton 3D printed from gypsum powder is microporous and permeable, with the experimentally determined mi-

croporosity $\phi_{\mathrm{m}} = 44\%$ and static permeability $\mathcal{K}_{0\mathrm{m}} = 1.64 \cdot 10^{-12}\,\mathrm{m}^2$. The micropores are very small compared to the slit width, which ensures a very good scale separation between the two pore networks, resulting in a dual porosity material. On the other hand, the skeleton of the resin sample is perfectly impermeable, which means that this panel has a single porosity, defined solely by the designed network of meandering slits.

2.2 Representative geometry

The panel samples have four slots on their front and back sides, see Figure 1. Each slot creates a continuous narrow channel that passes through the panel in a deliberately meandering fashion. In other words, the sample consists of four identical segments, each with a single slit channel that resembles a Greek meander pattern visible on the open lateral side of the panel made from transparent resin (Figure 1a). The gypsum panel sample is not transparent, so the invisible parts of the meander patterns (covered by the side struts that maintain the integrity of the sample) are drawn in dark grey in the photo of the open lateral side of this sample (Figure 1c).

Each panel segment is composed of $N_{\mathrm{r}} = 2$ rows of $N_{\mathrm{c}} = 2$ representative cells of the designed geometry shown in Figure 1b. Note that the second (upper) row is a mirrored copy of the first (lower) row. The cell is formed by two identical L-shaped parts of the skeleton, separated by the slit channel saturated with air. The width of the channel w is constant (between its bends) and together with the other three dimensions shown in Figure 1b, i.e. a_{L}, b_{L}, and c_{L}, fully defines the geometry of the cell. The cell width is $W_{\mathrm{c}} = 2c_{\mathrm{L}} + 2w$, while the entire width of the row or segment is $W_{\mathrm{r}} = N_{\mathrm{c}}W_{\mathrm{c}} + w + c_{\mathrm{L}}$, because each row also contains the outgoing part of the slit (width w) and one intersegmental partition (width c_{L}). The height of the row is the same as the cell height, i.e. $H_{\mathrm{r}} = 2a_{\mathrm{L}} + b_{\mathrm{L}} + w$, and the panel thickness is $H_{\mathrm{P}} = N_{\mathrm{r}}H_{\mathrm{r}}$.

The cell design can be considered generic and the proportions between dimensions can be changed, although a_{L}, b_{L}, and c_{L} should rather be larger than the slit width w. However, the proportions of the representative cell depicted in Figure 1b are actually the same as in the 3D printed samples. The corresponding values of basic dimensions (taken from the 3D printed specimens) are given in Table 1. Notice that the width of each sample is 2 mm larger than $4W_{\mathrm{r}}$. These 2 mm have been added so that the sample fits into a 66 mm square impedance tube. Note that excellent sealing is required around high-tortuosity samples as sound leakage can be a major potential source of discrepancy between predictions and measurements.

Table 1. Basic dimensions (mm).

w	a_{L}	b_{L}	c_{L}	W_{c}	W_{r}	H_{r}	H_{P}
1.40	1.55	8.00	1.80	6.40	16.0	12.5	25.0

3. ANALYTICAL MODELLING

3.1 Porosity, tortuosity, and characteristic lengths

Due to the relatively simple, essentially two-dimensional geometry of the slit pore network, analytical modelling can be applied. This is because the channels have a constant width and do not intersect – in fact there is only a single channel in each identical segment of the panel. Let s_{r} denote the total length of the channel inside a single row – then:

$$s_{\mathrm{r}} = N_{\mathrm{c}}s_{\mathrm{c}} + H_{\mathrm{r}}\,, \qquad s_{\mathrm{c}} = 2b_{\mathrm{L}} + 2c_{\mathrm{L}} + 2w\,, \tag{1}$$

where s_{c} is the length of the channel inside a single cell. The above definitions describe the length of the channel's central path with sharp bends or – and the same time – its length measured along one of the channel walls. Now, the porosity ϕ related to the slit network can be calculated as

$$\phi = A_{\mathrm{rf}}/A_{\mathrm{r}}\,, \quad A_{\mathrm{rf}} = s_{\mathrm{r}}w\,, \quad A_{\mathrm{r}} = W_{\mathrm{r}}H_{\mathrm{r}}\,, \tag{2}$$

where A_{rf} is the area of the fluid domain (i.e. channel) inside the cell and A_{r} is the total area of the cell. The dimensions specified for the entire geometry of the representative cell (see Figure 1b and Table 1) allow to determine the porosity $\phi = 40.1\%$.

Very important macro-parameter of acoustic materials with labyrinthine slits is their tortuosity. In order to determine it accurately, it is useful to consider first the channel's central line rounded at its turns with circular arcs (see Figure 1b). The length of this path across the entire row of the panel's segment $\breve{s}_{\mathrm{r}}$ is related to the path's length in a single cell $\breve{s}_{\mathrm{c}}$, which in turn can be computed by slightly modifying the length of the path with sharp bends s_{c}, namely

$$\breve{s}_{\mathrm{r}} = N_{\mathrm{c}}\breve{s}_{\mathrm{c}} + H_{\mathrm{r}} \qquad \breve{s}_{\mathrm{c}} = s_{\mathrm{c}} - 4w + \pi w\,. \tag{3}$$

The tortuosity is often treated as a geometric parameter and then usually defined as the squared ratio of the

average flow path length to the straight-line length across the porous medium [8, 9]. This definition can be used for porous networks with identical and not intersecting slits of constant width to analytically calculate the tortuosity as

$$\alpha_\infty = (N_\mathrm{r}\breve{s}_\mathrm{r}/H_\mathrm{P})^2 = (\breve{s}_\mathrm{r}/H_\mathrm{r})^2\,, \tag{4}$$

which for the considered geometry (see Figure 1b and Table 1) gives a relatively high value of $\alpha_\infty = 19.3$.

Characteristic lengths related to viscous flow and thermal diffusion effects are also required for further calculations and can be quickly determined for the considered network of identical slit channels. Since the slit width is constant, the viscous length Λ_v and thermal length Λ_th are both equal to it, i.e.

$$\Lambda_\mathrm{v} \approx \Lambda_\mathrm{th} = w\,. \tag{5}$$

This is an exact result in the case of Λ_th, while due to channel bends only a very accurate approximation in the case of Λ_v.

3.2 Single-porosity panel

In order to model acoustic panels in the time-harmonic regime depending on the angular frequency ω, the co-called dynamic viscous permeability $\mathcal{K}(\omega)$ and its thermal equivalent $\Theta(\omega)$ have to be calculated [10, 11]. These dynamic functions are complex-valued and can be expressed in terms of porosity, tortuosity, and characteristic lengths as follows

$$\mathcal{K}(\omega) = \Pi_\omega(\phi/\alpha_\infty, \Lambda_\mathrm{v}, \nu_\mathrm{a})\,, \tag{6}$$
$$\Theta(\omega) = \Pi_\omega(\phi, \Lambda_\mathrm{th}, \tau_\mathrm{a})\,, \tag{7}$$

where ν_a and τ_a are the kinematic viscosity and thermal diffusivity of the air saturating the labyrinthine slits, respectively, while the scaling function

$$\Pi_\omega(\psi, \Lambda, \mathcal{N}) = \frac{\psi\mathcal{N}}{\mathrm{i}\omega}\left(1 - \frac{\tanh\left(\frac{1}{2}\Lambda\sqrt{\mathrm{i}\omega/\mathcal{N}}\right)}{\frac{1}{2}\Lambda\sqrt{\mathrm{i}\omega/\mathcal{N}}}\right) \tag{8}$$

is based on the exact analytical solution derived for a straight slit [10], and modified only by introducing the tortuosity parameter in formula (6). Here and below, i denotes the imaginary unit.

One should notice that $\lim_{\omega\to 0}\Pi_\omega = \psi\Lambda^2/12$, which leads to the following well-known formulae for static – and therefore real-valued – viscous permeability $\mathcal{K}_0$ and thermal permeability Θ_0 of a material with slits [10]:

$$\mathcal{K}_0 \equiv \mathcal{K}(0) = \frac{\phi\Lambda_\mathrm{v}^2}{12\alpha_\infty}\,, \quad \Theta_0 \equiv \Theta(0) = \frac{\phi\Lambda_\mathrm{th}^2}{12}\,. \tag{9}$$

When these two parameters are known, the dynamic permeabilities $\mathcal{K}(\omega)$ and $\Theta(\omega)$ can alternatively be calculated using the well-known Johnson-Champoux-Allard-Lafarge (JCAL) model [10], which is a more versatile approximation, but for the considered panels gives practically the same results as the formula (8) derived for slits.

The dynamic thermal permeability $\Theta(\omega)$ is used to calculate the effective compressibility of the single-porosity panel (3D printed from resin), namely

$$\mathcal{C}_\mathrm{sg}(\omega) = \frac{\phi}{P_0}\left(1 - \frac{\gamma_\mathrm{a} - 1}{\gamma_\mathrm{a}}\frac{\Theta(\omega)}{\phi\,\tau_\mathrm{a}}\mathrm{i}\omega\right)\,, \tag{10}$$

where P_0 is the ambient mean pressure and γ_a is the heat capacity ratio for air.

3.3 Dual-porosity panel

The skeleton of the material 3D printed from gypsum powder is microporous. However, its viscous permeability $\mathcal{K}_{0\mathrm{m}} = 1.64\cdot 10^{-12}\mathrm{m}^2$ is much lower than the permeability $\mathcal{K}_0 = 3.40\cdot 10^{-9}\mathrm{m}^2$ associated with the network of labyrinthine slits, i.e. $\mathcal{K}_{0\mathrm{m}} \ll \mathcal{K}_0$, which not only ensures an excellent scale separation between the networks of micropores and main pores (slits), but also provides an additional effect to dissipate the energy of airborne acoustic waves, namely the pressure diffusion occurring due to such a high permeability contrast [4].

The pore scale separation means that the oscillating viscous airflow caused by the acoustic wave propagating in dual-porosity materials is mainly confined to the main pore network – of labyrinthine slits in the studied case. Therefore, the dynamic viscous permeability $\mathcal{K}(\omega)$ for the dual-porosity material 3D printed from gypsum powder is practically the same as in the case of single-porosity material 3D printed from resin, because any surface roughness and other imperfections are neglected in the modelling.

On the other hand, the dual-porosity effect must be taken into account when determining the effective compressibility, because pressure variations in the micropores cannot be neglected.

Let ϕ_d denote the volume fraction of the microporous domain. In the gypsum-based panel the entire skeleton is microporous so $\phi_\mathrm{d} = 1 - \phi = 59.9\%$, and the total porosity is $\phi + \phi_\mathrm{d}\phi_\mathrm{m} = 66.5\%$. In dual-porosity materials, the effective compressibility $\mathcal{C}_\mathrm{db}(\omega)$ is calculated as the sum of the compressibility $\mathcal{C}_\mathrm{sg}(\omega)$ obtained for the main pore network and the contribution related to the microporous network. The latter must be modified by function $\mathcal{F}_\mathrm{d}(\omega)$ to take into account the phenomenon of pressure diffusion,

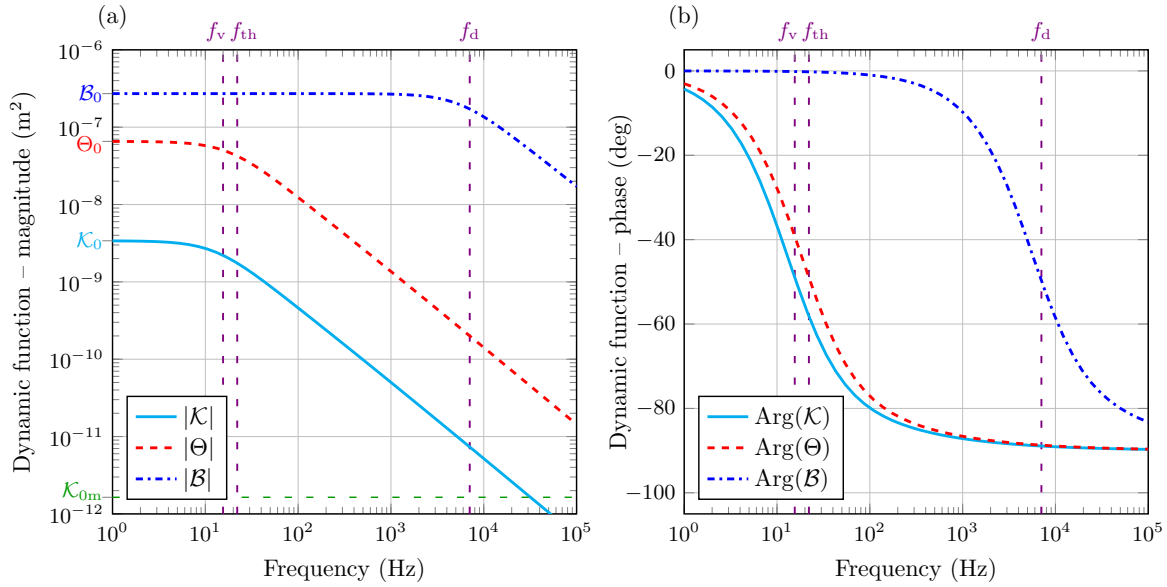

Figure 2. Dynamic functions of viscous and thermal permeability and pressure diffusion: (a) magnitude, and (b) phase.

occurring in the considered case of high permeability contrast [4]. Therefore,

$$\mathcal{C}_{db}(\omega) = \mathcal{C}_{sg}(\omega) + \phi_d \mathcal{F}_d(\omega) \frac{\phi_m}{P_0}\,, \tag{11}$$

where the term ϕ_m/P_0 is the effective compressibility of air in the micropores, and the function

$$\mathcal{F}_d(\omega) = 1 - \frac{\mathcal{B}(\omega)}{\phi_d \mathcal{D}_{0m}} i\omega \tag{12}$$

describes the ratio of the averaged pressure locally fluctuating in the microporous skeleton to the locally-constant pressure [4, 11] in the representative part of the slit channel. In the formula (12),

$$\mathcal{D}_{0m} = \frac{\mathcal{K}_{0m}}{\phi_m \eta_a} \tag{13}$$

is the pressure diffusivity of the microporous material, which in particular depends on the dynamic viscosity of air η_a, while $\mathcal{B}(\omega)$ is the dynamic pressure diffusion function which can be calculated using the JCAL model [4, 10, 11] – the required parameters are: $\mathcal{D}_{0m}$, ϕ_d, as well as the associated characteristic length Λ_d and static pressure diffusion $\mathcal{B}_0$.

The characteristic length related to the pressure diffusion in dual-porosity material can be calculated as

$$\Lambda_d = \Lambda_{th}\phi_d/\phi = w\phi_d/\phi\,, \tag{14}$$

while the static pressure diffusion $\mathcal{B}_0$ is the average of the solution of a specific Poisson problem for diffusion defined in the microporous domain of the representative cell [4, 11]. However, for the microporous skeleton shown in Figure 1b, this parameter can also be approximately calculated as

$$\mathcal{B}_0 \equiv \mathcal{B}(0) = \frac{\phi_d \Lambda_d^2}{\zeta_d}\,, \tag{15}$$

where ζ_d is roughly estimated assuming an equivalent rectangular microporous domain (therefore, $7.11 < \zeta_d < 12$). For the considered shape of the microporous skeleton, this value was determined as $\zeta_d = 9.64$ – from the curve shown in Figure 10 in [12] – assuming that the equivalent rectangular proportions are b_L/c_L.

3.4 Dynamic functions and effective properties

The dynamic functions that have been calculated for the materials studied in this work are presented in Figure 2 – over a wide range of frequencies to fully show the nature of these curves, i.e. for $f = \omega/(2\pi)$ such that $1\,\text{Hz} \le f \le 100\,\text{kHz}$, although the modelling is valid

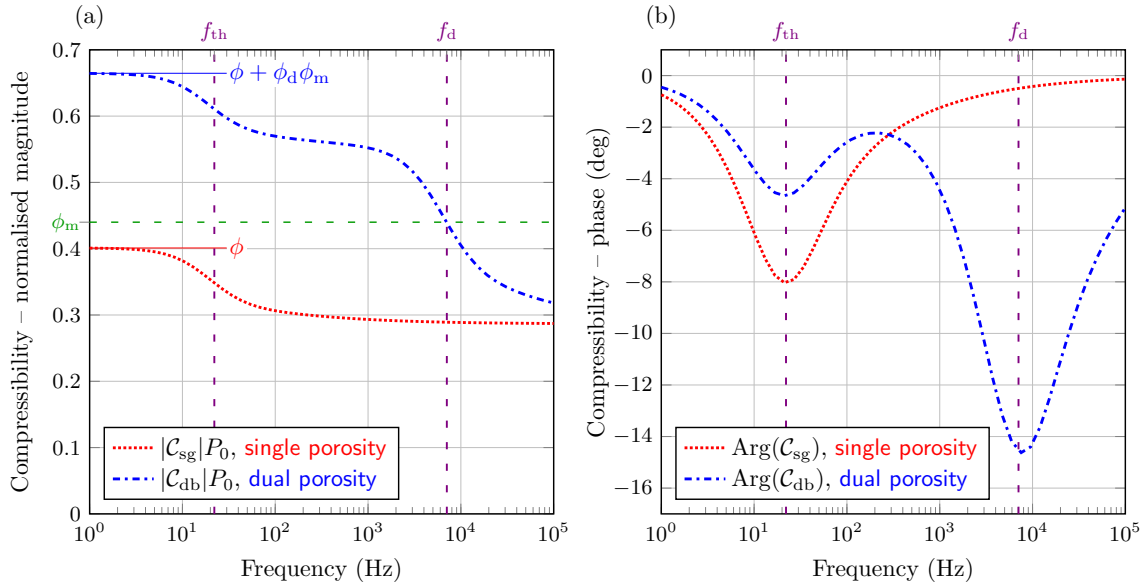

Figure 3. Effective compressibility for the single- and dual-porosity panels: (a) normalised magnitude, and (b) phase.

for $f < 10\,\mathrm{kHz}$. Figure 2a shows the magnitude, i.e. the absolute value of the dynamic viscous and thermal permeabilities as well as dynamic pressure diffusion. Their static values, i.e. $\mathcal{K}_0$, Θ_0, and $\mathcal{B}_0$, respectively, are marked on the vertical axis, along with the static viscous permeability of the microporous material $\mathcal{K}_{0\mathrm{m}}$, which in practice can replace the dynamic permeability of this material. The huge difference, i.e. the aforementioned contrast between $\mathcal{K}_0$ and $\mathcal{K}_{0\mathrm{m}}$ is easily seen. For completeness, the phases of the dynamic functions are shown in Figure 2b. Note that the characteristic features of each of the curves occur around their specific characteristic frequencies: f_{v}, f_{th}, and f_{d}, associated with the viscous, thermal, and pressure diffusion effects, respectively. These frequencies are defined by the following relations [4]

$$2\pi f_{\mathrm{v}} = \frac{\phi\,\nu_{\mathrm{a}}}{\mathcal{K}_0\alpha_\infty}, \quad 2\pi f_{\mathrm{th}} = \frac{\phi\,\tau_{\mathrm{a}}}{\Theta_0}, \quad 2\pi f_{\mathrm{d}} = \frac{\phi_{\mathrm{d}}\mathcal{D}_{0\mathrm{m}}}{\mathcal{B}_0}, \tag{16}$$

which – in the considered case, i.e. when the formulae (9) and (15) are valid – reduce to

$$f_{\mathrm{v}} = \frac{6\nu_{\mathrm{a}}}{\pi\Lambda_{\mathrm{v}}^2}, \qquad f_{\mathrm{th}} = \frac{6\tau_{\mathrm{a}}}{\pi\Lambda_{\mathrm{th}}^2}, \qquad f_{\mathrm{d}} = \frac{\zeta_{\mathrm{d}}\mathcal{D}_{0\mathrm{m}}}{2\pi\Lambda_{\mathrm{d}}^2}. \tag{17}$$

Figure 3 shows the effective compressibility determined for the single- and dual-porosity materials. The magnitude of the effective compressibility – see Figure 3a – is normalised, i.e. divided by the isothermal compressibility of air which equals to $1/P_0$. Note that in the case of single porosity $\lim_{\omega\to 0}\mathcal{C}_{\mathrm{sg}}(\omega)P_0 = \phi$, while for the dual-porosity material $\lim_{\omega\to 0}\mathcal{C}_{\mathrm{db}}(\omega)P_0 = \phi + \phi_{\mathrm{d}}\phi_{\mathrm{m}}$, which means that the static value of the normalised effective compressibility is always equal to the total porosity.

The phase of the effective compressibility is compared in Figure 3b for the single- and dual-porosity materials. Both curves have local extrema around the characteristic frequency f_{th} associated with the thermal diffusion in slits. However, the effective compressibility phase of the dual-porosity material reaches an additional extreme value around the characteristic frequency f_{d} related to the pressure diffusion.

The dynamic viscous permeability and effective compressibility allow to determine the effective density $\varrho_{\mathrm{e}}(\omega)$ and speed of sound $c_{\mathrm{e}}(\omega)$ of porous materials, namely

$$\varrho_{\mathrm{e}}(\omega) = \frac{\eta_{\mathrm{a}}}{\mathrm{i}\omega\mathcal{K}(\omega)}, \qquad c_{\mathrm{e}}(\omega) = \sqrt{\frac{\mathrm{i}\omega\mathcal{K}(\omega)}{\eta_{\mathrm{a}}\,\mathcal{C}(\omega)}}, \tag{18}$$

where $\mathcal{C}(\omega) = \mathcal{C}_{\mathrm{sg}}(\omega)$ for the material with a single porosity, and $\mathcal{C}(\omega) = \mathcal{C}_{\mathrm{db}}(\omega)$ for the dual-porosity material. Recall that due to the high permeability contrast in the latter, $\mathcal{K}(\omega)$ and therefore also $\varrho_{\mathrm{e}}(\omega)$ are the same for both materials, only $c_{\mathrm{e}}(\omega)$ is different. However, this is enough to

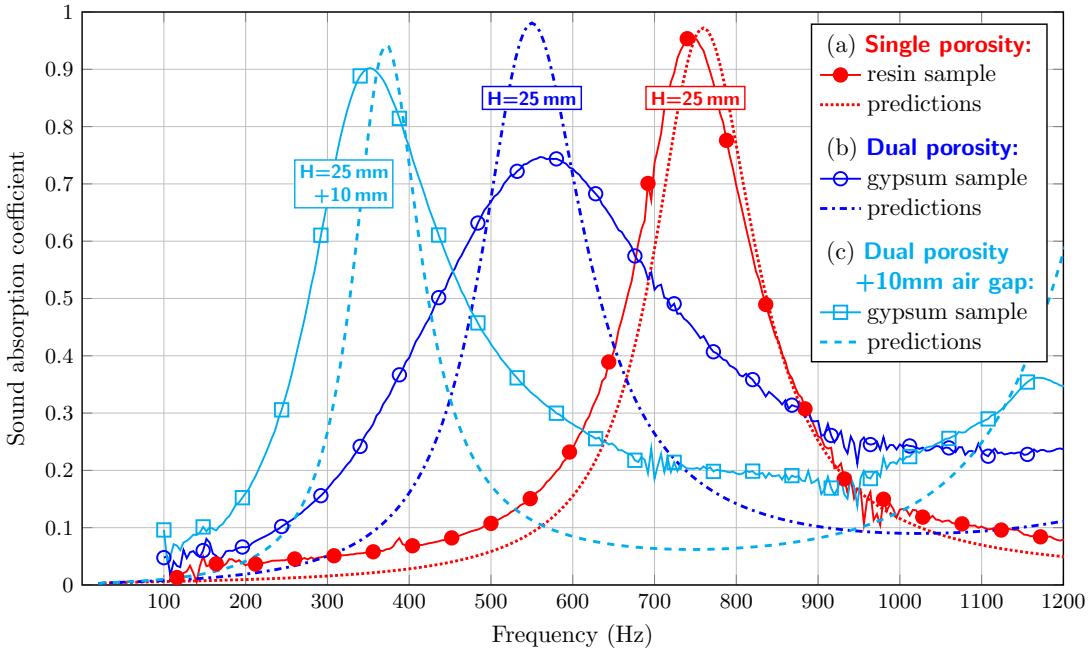

Figure 4. Measured and predicted normal incidence sound absorption by 25 mm thick single- and dual-porosity panels with a hard backing, and – in the latter case – also with a 10 mm air gap.

make the effective characteristic impedance of these materials, $Z_e(\omega) = \varrho_e(\omega)\, c_e(\omega)$, significantly different when dealing with the single- or dual-porosity case.

4. SOUND ABSORPTION

Figure 4 shows the sound absorption curves measured in a 66 mm square impedance tube for both 3D printed panel samples. These absorption curves (solid lines with markers) are compared with the corresponding analytical predictions (lines without markers). The sound absorption coefficient is calculated as [10]

$$\mathcal{A}(\omega) = 1 - \left| \frac{Z_s(\omega) - Z_a}{Z_s(\omega) + Z_a} \right|^2 \qquad (19)$$

where Z_a is the characteristic impedance of air, and $Z_s(\omega)$ is the surface impedance of the absorbing layer.

The sound absorption of the single-porosity panel was measured for the resin sample backed directly by a rigid piston, and in analytical modelling, the surface impedance $Z_s(\omega)$ was calculated for such a 25 mm panel backed by a rigid wall from a well-known analytical formula that requires $Z_e(\omega)$, $c_e(\omega)$, and H_P [10]. The sound absorption predictions for this panel agree very well with the measurements – cf. red curves in Figure 4. In the frequency range of interest, i.e. below 1.2 kHz, nearly perfect absorption is achieved at about 750 Hz, however, the absorption coefficient still exceeds 0.4 over a fairly wide frequency range around this peak, i.e. from about 650 Hz to 850 Hz.

The sound absorption calculations for the dual-porosity panel predicted that the absorption peak should be shifted to a much lower frequency of 550 Hz, while the frequency span of decent absorption around the peak is preserved. These predictions were only qualitatively confirmed by the measurements – cf. blue curves in Figure 4 – possibly due to sample imperfections and sound leakage. The measured sound absorption is only 0.75 at the peak, but on the other hand, the frequency range of decent (i.e. more than 0.4) absorption is almost twice as wide, namely from 400 Hz to almost 800 Hz, which may be more desirable in applications. For further verification of the case of dual porosity, the sound absorption was also measured for the gypsum-based panel in another configuration, namely with a 10 mm air gap between the sample and the backing rigid wall. The total thickness of such a two-layer configuration is $H = H_P + 10\,\text{mm} = 35\,\text{mm}$, and the peak absorption is 0.9 at a very low frequency of about 350 Hz. These

measurement results are in fairly good agreement with the analytical predictions – cf. cyan (light blue) curves in Figure 4 – for which the surface impedance $Z_s(\omega)$ was calculated using formulae derived for the two-layer configuration [10].

5. CONCLUSIONS

3D printed samples of panels with labyrinthine slits allowed to experimentally demonstrate the great potential of such highly-tortuous acoustic material designs. It is worth mentioning here that the slit network geometry was not optimised – in particular, the slit width was wider than necessary to facilitate the removal of gypsum powder residue. It is envisaged that narrower slits should provide at least similar performance, even though the panels are thinner. Experimental results confirmed the sound absorption predicted by the developed analytical models, in particular very accurately for the single-porosity panel. Discrepancies between the sound absorption predictions and measurements for the hard backed dual-porosity panel can be attributed to sound leakages around this sample as well as its imperfections, including inhomogeneity and anisotropy of the microporous network.

6. ACKNOWLEDGMENTS

This research was financially supported by the National Science Centre (NCN), Poland, as part of the project "Sound-absorbing composites: coupled acoustic energy dissipation mechanisms, multiscale modelling and prototyping", under Grant Agreement No. 2021/41/B/ST8/04492.

7. REFERENCES

[1] K. Attenborough, "Microstructures for lowering the quarter wavelength resonance frequency of a hard-backed rigid-porous layer," *Applied Acoustics*, vol. 130, pp. 188–194, 2018.

[2] I. Prasetiyo, K. Anwar, F. Brahmana, and K. Sakagami, "Development of stackable subwavelength sound absorber based on coiled-up system," *Applied Acoustics*, vol. 195, p. 108842, 2022.

[3] K. Attenborough, "Analytical approximations for sub wavelength sound absorption by porous layers with labyrinthine slit perforations," *Applied Sciences*, vol. 11, p. 3299, 2021.

[4] X. Olny and C. Boutin, "Acoustic wave propagation in double porosity media," *The Journal of the Acoustical Society of America*, vol. 114, pp. 73–89, 2003.

[5] I. Gibson, D. Rosen, and B. Stucker, *Additive Manufacturing Technologies: 3D Printing, Rapid Prototyping, and Direct Digital Manufacturing*. Springer, New York, 2 ed., 2015.

[6] T. G. Zieliński, K. C. Opiela, P. Pawłowski, N. Dauchez, T. Boutin, J. Kennedy, D. Trimble, H. Rice, B. Van Damme, G. Hannema, R. Wróbel, S. Kim, S. Ghaffari Mosanenzadeh, N. X. Fang, J. Yang, B. Briere de La Hosseraye, M. C. Hornikx, E. Salze, M.-A. Galland, R. Boonen, A. Carvalho de Sousa, E. Deckers, M. Gaborit, and J.-P. Groby, "Reproducibility of sound-absorbing periodic porous materials using additive manufacturing technologies: Round robin study," *Additive Manufacturing*, vol. 36, p. 101564, 2020.

[7] A. Ciochon, J. Kennedy, R. Leiba, L. Flanagan, and M. Culleton, "The impact of surface roughness on an additively manufactured acoustic material: An experimental and numerical investigation," *Journal of Sound and Vibration*, vol. 546, p. 117434, 2023.

[8] P. C. Carman, "Fluid flow through granular beds," *Transactions of the Institution of Chemical Engineers (London)*, vol. 15, pp. 150–166, 1937. Reprinted in: *Chemical Engineering Research and Design*, vol. 75, Supplement, pp. S32-S48, 1997.

[9] B. Ghanbarian, A. G. Hunt, R. P. Ewing, and M. Sahimi, "Tortuosity in porous media: A critical review," *Soil Science Society of America Journal*, vol. 77, pp. 1461–1477, 2013.

[10] J. F. Allard and N. Atalla, *Propagation of Sound in Porous Media: Modeling Sound Absorbing Materials, 2nd ed.* John Wiley & Sons, Chichester, 2009.

[11] T. G. Zieliński, N. Dauchez, T. Boutin, M. Leturia, A. Wilkinson, F. Chevillotte, F.-X. Bécot, and R. Venegas, "Taking advantage of a 3D printing imperfection in the development of sound-absorbing materials," *Applied Acoustics*, vol. 197, p. 108941, 2022.

[12] T. G. Zieliński, F. Chevillotte, and E. Deckers, "Sound absorption of plates with micro-slits backed with air cavities: Analytical estimations, numerical calculations and experimental validations," *Applied Acoustics*, vol. 146, pp. 261–279, 2019.